nature communications

Article

https://doi.org/10.1038/s41467-025-56190-5

Engineering triple O-Ti-O vacancy associates for efficient water-activation catalysis

Received: 29 May 2024

Accepted: 10 January 2025

Published online: 20 January 2025

Check for updates

Feng Bi[1,10], Qingjie Meng[2,10], Yili Zhang[3], Hao Chen[4], Boqiong Jiang[5], Hanfeng Lu[6], Qinghua Liu[7], Hongjun Zhang[4], Zhongbiao Wu[1,8] & Xiaole Weng[1,8,9]

Defect engineering can create various vacancy configurations in catalysts by finely tuning the local electronic and geometric structures of the active sites. However, achieving precise control and identification of these defects remains a significant challenge, and the origin of vacancy configurations in catalysts, especially clustered or associated ones, remains largely unknown. Herein, we successfully achieve the controllable fabrication and quantitative identification of triple O-Ti-O vacancy associate ($V_OV_{Ti}V_O$) in nanosized Ni-doped TiO_2. Experimental and theoretical analyses demonstrate that terminal hydroxyls adsorbed at unsaturated cationic sites play an essential role in boosting $V_OV_{Ti}V_O$ formation, which enhances H_2O dissociation and facilitates dissociative OH* deprotonation for defect site regeneration. In contrast, a single V_O can be easily saturated by dissociative bridging hydroxyl accumulation, leading to a gradual decrease in the number of active sites. The essential role of $V_OV_{Ti}V_O$ in the Ni-doped TiO_2 is evidenced by its comparable catalytic performance in the hydrogen evolution reaction and hydrodechlorination reactions. Our work highlights the importance of engineering vacancy-associated active sites and presents a notable approach for designing highly active and selective catalysts for efficient H_2O-involved reactions.

Defects play a critical role in catalysis due to their unsaturated coordination and distinct reactivity[1–9]. Engineering defects in catalysts can reduce the coordination number of neighboring atoms and create enriched unsaturated sites essential for the adsorption and activation of reactant molecules. While single defects have received considerable attention, recent research has increasingly focused on clustered/associated defect engineering[10–12]. This growing interest indicates that the type (e.g., mono, dimer, or triple) and relative abundance of different defects can be intentionally adjusted to finely adjust the local electronic and geometric structure of active sites, thereby altering the electron donor/acceptor capabilities of catalysts during reactant activation. In a recent study by Guan et al., it was reported that a triple vacancy associate ($V_{Bi}V_OV_{Bi}$) formed by dimensionally tuning BiOCl nanosheets not only increased the adsorption capacity of reactants but also promoted the separation of electron−hole pairs, resulting in a substantial enhancement of solar-driven photocatalytic activity[13]. Similarly, Wei et al. discovered that engineering clustered oxygen vacancies on titanium-based perovskites greatly enhanced the H_2O

[1]College of Environmental and Resource Sciences, Zhejiang University, Hangzhou, PR China. [2]School of Civil & Environmental Engineering and Geography Science, Ningbo University, Ningbo, PR China. [3]Shanghai Academy of Environmental Sciences, Shanghai, PR China. [4]State Key Laboratory of Particle Detection and Electronics, University of Science and Technology of China, Hefei, PR China. [5]School of Environmental Science and Engineering, Zhejiang Gongshang University, Hangzhou, PR China. [6]Institute of Catalytic Reaction Engineering, College of Chemical Engineering, Zhejiang University of Technology, Hangzhou, PR China. [7]National Synchrotron Radiation Laboratory, University of Science and Technology of China, Hefei, PR China. [8]Zhejiang Provincial Key Laboratory of Air Pollution Monitoring and Synergistic Control, Hangzhou, PR China. [9]ZJU-Hangzhou Global Scientific and Technological Innovation Center, Hangzhou, PR China. [10]These authors contributed equally: Feng Bi, Qingjie Meng. e-mail: xlweng@zju.edu.cn

dissociation capability, enabling lower-temperature hydrolysis of organic sulfur compounds[14]. Despite the promising outcomes associated with various defect configurations, engineering these active sites at a level where their types and relative abundances can be controlled and precisely identified remains a significant challenge. This challenge stems from their structural diversity, high formation energy, and relative instability. Moreover, the origin of these defect configurations in the different types of catalysts, particularly the clustered/associated ones, has rarely been explored.

The activation of H_2O molecules serves as a key fundamental step in various important chemical reactions, such as the water-gas shift reaction, steam reforming, and photocatalytic hydrogen generation[14–16]. Understanding the process of water activation at defects is a crucial topic in surface science, energy, and catalysis. Continual H_2O activation generally involves inert H_2O dissociation and subsequent active site regeneration, whereas the presence of anionic defects, e.g., oxygen vacancies in metal oxides, can greatly facilitate H_2O dissociation[1]. However, the strong binding of dissociated hydroxyl groups (OH*) at these defects tends to deplete such active sites, resulting in irreversible surface reconstruction and catalyst deactivation[17–19]. In contrast, cationic defects, such as the Co defect (V_{Co}) in Co_3O_4, can enhance the deprotonation of OH*, which originates from the hydrogen bonds between V_{Co}-activated O_{2f} and H atoms of intermediates (OH*, OOH*) that decrease the deprotonation energy barrier[19]. Considering the advancements in anionic and cationic defects for H_2O dissociation and OH* deprotonation, respectively, it can be expected that engineering cation–anion vacancy associates in catalysts may promote H_2O dissociation and defect site regeneration, thereby enabling efficient water-activation catalysis.

Herein, we developed a notable engineering strategy to fabricate cation–anion defect associations in nanosized anatase TiO_2, a well-known semiconductor catalyst since 1972[20]. By introducing atomically dispersed nickel atoms into surface organic-coated anatase TiO_2, followed by calcination in either N_2 or air atmosphere, the predominant types and relative abundance of defects in Ni-doped TiO_2 were deliberately manipulated, transitioning from single oxygen vacancies to anion–cation vacancy associates. We found that this controlled manipulation mainly stems from the diverse hydroxyl groups (i.e., acidic bridging and basic terminal groups) bonded to the TiO_2 surface originating from the oxidation of surficial organics during annealing. We demonstrate that annealing organic-coated Ni-doped TiO_2 in air can produce abundant anion–cation $V_OV_{Ti}V_O$ associates that enhance H_2O dissociation and facilitate dissociative OH* deprotonation for active site regeneration. Consequently, this catalyst exhibited a continual H_2O activation ability, showing significantly higher catalytic activities in the hydrogen evolution reaction (HER, 3.3-fold greater) and hydrodechlorination (HDC, 6.8-fold greater) than Ni-TiO_2 with single oxygen vacancies. Insights into the formation of various defect types and the resulting changes in the local coordination and physicochemical properties of Ni-doped TiO_2 were obtained through positron annihilation lifetime spectroscopy (PALS), X-ray absorption fine structure (XAFS) analysis, and quasi in situ X-ray photoelectron spectroscopy (quasi in situ XPS) measurements, which were further corroborated by density functional theory (DFT) calculations.

Results

Synthesis and characterization

Atomically dispersed nickel dopant on TiO_2 was fabricated using a continuous hydrothermal flow synthesis (CHFS) route (Supporting Information, Fig. S1)[21–23]. Briefly, an aqueous precursor solution containing titanium (IV) bis(ammonium lactate) dihydroxide (TiBALD) and $Ni(NO_3)_2{\cdot}6H_2O$ was mixed with supercritical water (sc-H_2O) at 450 °C (supercritical temperature Tc = 374 °C, pressure Pc = 22.1 MPa) in a confined jet mixer. Upon cooling in flow, an aqueous slurry of organic-coated Ni-doped TiO_2 (denoted as Ni-TiO_2) nanoparticles (NPs) was obtained. Subsequent defect engineering was accomplished by aging the pristine Ni-TiO_2 NPs under either air or N_2 atmosphere at 300 °C for 2 h (a flow rate of 100 mL min^{-1}). The resulting samples were labelled Ni-TiO_2-Air and Ni-TiO_2-N_2, respectively (Fig. 1a). The actual Ni loading in the pristine sample and annealed samples (air or N_2) were determined using X-ray fluorescence spectrometry, confirming that the Ni loading was ~1 mol%, as expected (Table S1).

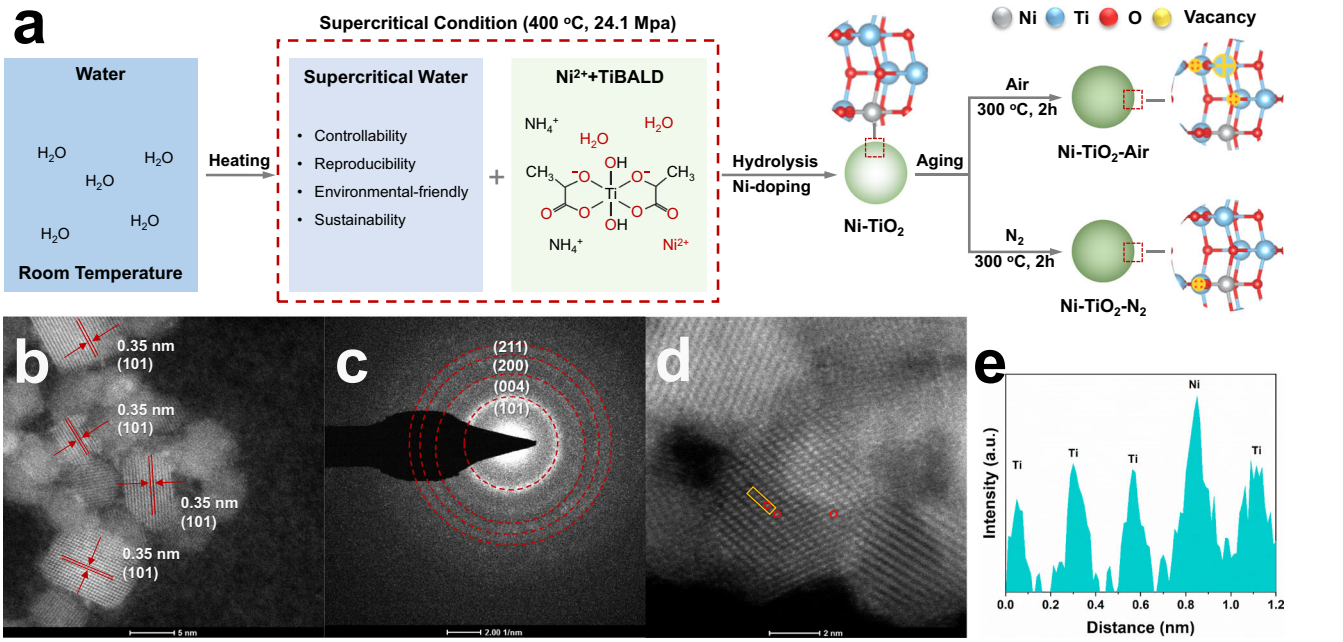

Fig. 1 | Schematic illustration and morphology characterization of catalysts. **a** Schematic diagram for preparing the Ni-TiO_2, Ni-TiO_2-Air and Ni-TiO_2-N_2 samples. **b** High-resolution transmission electron microscopy (HR-TEM) image and **c** corresponding selected area electron diffraction (SAED) pattern of Ni-TiO_2. **d** Aberration-corrected high-angle annular dark-field scanning transmission electron microscopy (AC HAADF-STEM) image of Ni-TiO_2 (Ni single sites are marked by red cycles). **e** Corresponding line intensity profile taken along the yellow rectangle in panel **d** (a.u. = arbitrary units).

The phase and structural characteristics of the pristine and annealed Ni-TiO_2 samples were analyzed by X-ray powder diffraction (XRD) and high-resolution transmission electron microscopy (HR-TEM). XRD data for all the samples (Supporting Information, Fig. S2) showed characteristic peaks corresponding to the pure anatase TiO_2 structure (JCPDS No. 21-1272)[22]. No detectable reflections for Ni-related compounds, including metallic Ni and NiO NPs, were observed. Further Rietveld refinement confirmed that the Ni atoms were fully incorporated into the TiO_2 lattice through cationic substitution. As shown in Supplementary Fig. S3 and Table S2, the refinement of pristine Ni-TiO_2 gave a satisfactory fit to tetragonal $Ni_{0.01}Ti_{0.99}O_2$ (R_{wp} = 0.22) in space group I41/amd with elongated axes compared to undoped CHFS-made TiO_2. The presence of the Ni dopant led to an expansion of the TiO_2 lattice, with the unit cell volume slightly changing from 136.7 $Å^3$ to 137.7 $Å^3$. This is unsurprising given the relatively larger Ni^{2+} ion radius (0.069 nm) than those of Ti^{4+} (0.0605 nm) and Ti^{3+} (0.067 nm). Notably, annealing in either air or N_2 resulted in a contraction of the Ni-TiO_2 lattice, leading to shortened axes. The formation of defects during annealing should account for this shrinkage. Moreover, different annealing atmospheres influence the defect configurations since the *a*- and *b*-axes of Ni-TiO_2-Air are shorter, whereas the *c*-axis is longer than that of Ni-TiO_2-N_2. The HR-TEM image (Fig. 1b) and corresponding selected area electron diffraction (SAED) pattern (Fig. 1c) showed no Ni clusters or NiO NPs in Ni-TiO_2, confirming the absence of metallic Ni or NiO, which is consistent with the XRD and Raman results (Supporting Information, Figs. S2–S4). Further energy-dispersive X-ray spectroscopy elemental mapping (Supporting Information, Fig. S5) confirmed that the Ni atoms were well dispersed in TiO_2. Moreover, the aberration-corrected high-angle annular dark-field scanning transmission electron microscopy (AC HAADF-STEM) was adopted to reveal the dispersion of the Ni sites in the TiO_2 lattice (Fig. 1d). The intensity profile (Fig. 1e) from the area (marked by a yellow rectangle in Fig. 1d) confirmed the formation of isolated Ni single site, indicating that highly dispersed Ni remained confined within the TiO_2 lattice. The well-preserved morphology of both the pristine and annealed Ni-TiO_2 samples was consistent with their slightly changed surface areas, ranging from 232 to 247 $m^2 g^{-1}$ (Table S3).

Accurately identifying and quantifying various defects in pristine and annealed Ni-TiO_2 samples are essential for a thorough understanding of their catalytic functions. Electron paramagnetic resonance (EPR) measurements were first performed to probe the presence and relative abundance of defects in each sample. As depicted in Fig. 2a, all the samples exhibited an EPR signal at g = 2.002, indicating the presence of unpaired electrons trapped at oxygen vacancies. The strongest signal observed for Ni-TiO_2-N_2 indicated the presence of abundant oxygen vacancies in the sample. Interestingly, Ni-TiO_2-Air displayed an additional EPR signal at g = 1.99, corresponding to titanium vacancies, and g = 1.97, commonly associated with Ti^{3+} centers in TiO_2[24,25]. This suggests that different vacancy configurations are induced by different annealing atmospheres. PALS combined with DFT calculations were further used to accurately identify the types of defects in each sample. As illustrated in Table 1 and Fig. S6, all the samples exhibited three distinct lifetime components (τ_1, τ_2, and τ_3) in their PALS profiles. The shortest peak (τ_1, ~250 ps) is assigned to positrons trapped in the defect-free region and smaller defects (e.g., monovacancies and vacancy associates), the intermediate peak (τ_2, 350-550 ps) corresponds to large vacancy clusters in crystallites and grain boundary regions, and the longest peak (τ_3, 5-15 ns) is attributed to orthopositronium atom annihilation in large voids and/or at the interface. Based on theoretical calculations using a $Ti_{48}O_{96}$ model (Supporting Information, Table S4 and Fig. S7), the predominant defects in Ni-TiO_2-Air with a τ_1 of 232.3 ± 4.1 ps are attributed to associated O–Ti–O trimer vacancies (denoted $V_OV_{Ti}V_O$), and those in Ni-TiO_2 (197.8 ± 2.2 ps) and Ni-TiO_2-N_2 (197.7 ± 4.5 ps) are attributable to isolated monovacancy (V_O, V_{Ti}) or O–O(-O) oxygen vacancy associates (V_OV_O or $V_OV_OV_O$), with predicted lifetimes ranging from 189.8-199.0 ps. To further distinguish these defect configurations, their formation energies (E_{vac}) were calculated. As shown in Fig. 2b and Fig. S8, the E_{vac} of a mono oxygen vacancy (V_O) in the $Ti_{24}O_{28}$ slab was calculated to be 4.10 eV, which is significantly lower than that of a dimer vacancy (V_OV_O, 10.30 eV), trimer vacancy ($V_OV_OV_O$, 15.91 eV), or mono titanium vacancy (V_{Ti}, 15.24 eV). Notably, the E_{vac} of the V_O adjacent to the Ni atom decreased drastically to 0.6 eV, indicating that mono V_O can be readily generated in Ni-TiO_2. These results suggested that the predominant defects in Ni-TiO_2 and Ni-TiO_2-N_2 could be isolated monovacancies (V_O, Figs. 2c and S9), as other oxygen vacancy associates (dimers or trimers) or isolated Ti vacancies were unlikely to form because of their extremely high formation energies, even with Ni doping. For $V_OV_{Ti}V_O$, the E_{vac} in the $NiTi_{23}O_{28}$ slab was calculated to be 6.92 eV, which is relatively lower than that in $Ti_{24}O_{28}$ (at 7.58 eV). This indicates that generating $V_OV_{Ti}V_O$ associates in TiO_2 is also challenging. We propose that surface organic coating could play an essential role in facilitating the generation of $V_OV_{Ti}V_O$ associates in Ni-TiO_2-Air, as the CHFS-made organic-coated TiO_2 treated in air also exhibited predominant $V_OV_{Ti}V_O$ associates (τ_1 = 231.8 ± 3.7 ps) but with a much lower relative intensity (I_1/I_2) of 0.16 than that of Ni-TiO_2-Air (I_1/I_2 = 0.95). In contrast, standard anatase TiO_2 (i.e., without an organic coating) treated in air did not yield any such vacancy associates[26].

Quasi in situ XPS analysis was performed on pristine Ni-TiO_2 to confirm the change in the chemical state of Ni species upon annealing (Supporting Information, Fig. S10). Compared with the pristine Ni-TiO_2 sample and the N_2 annealed sample (labeled as "N_2 300 °C 2 h" in Fig. S10), the Ni $2p_{3/2}$ peak of the air annealed sample (labeled as "Air 300 °C 2 h" in Fig. S10) showed a lower binding energy (BE) shift to 855.0 eV, which indicated a reduced Ni valence state upon air annealing[27]. XAFS spectroscopy was further performed to investigate the local coordination environments of Ni and Ti in each sample. As shown in Fig. 3a, the Ni K-edge X-ray absorption near-edge structure (XANES) spectra revealed that the absorption edge position of each sample shifted towards higher energies compared to that of NiO, indicating that Ni atoms predominantly carried positive charges, with their valence states primarily above +2, suggesting the presence of NiOOH or Ni_2O_3 in the Ni-TiO_2 samples. Notably, the absorption edge of Ni-TiO_2-Air shifted to a lower energy than that of Ni-TiO_2, a typical indication of valence-state variation from high oxidation Ni(III) to reduced Ni(II). This indicated that annealing in air increased the local electron density of the Ni atoms and decreased their valence state.

Moreover, Fourier transform of extended X-ray absorption fine structure (FT-EXAFS) spectra (Fig. 3b) indicated that the Ni-TiO_2, Ni-TiO_2-Air, and Ni-TiO_2-N_2 samples all displayed predominant coordination at 1.6 Å, corresponding to Ni–O bonds[28]. No obvious peak corresponding to either the Ni–Ni shell (2.2 Å) or the Ni–O–Ni shell (Ni–Ni in NiO, 2.7 Å) was observed, suggesting that the Ni atoms were atomically dispersed[29], which is consistent with the Rietveld refinement and AC HADDF-STEM results. Further EXAFS wavelet transform (WT) analysis discriminated the backscattering atoms (Fig. 3c), and a predominant peak assigned to the Ni–O scattering path at ~6 $Å^{-1}$ was observed[30]. This result confirms the atomic dispersion of the Ni atoms in the TiO_2 lattice. The FT-EXAFS spectra in R-space were analyzed to determine the coordination environment of Ni in each sample (Supporting Information, Fig. S11 and Table S5), revealing that the coordination numbers of the Ni–O first shell for the Ni-TiO_2, Ni-TiO_2-Air, and Ni-TiO_2-N_2 samples were 6.00, 5.31 and 5.96, respectively. Additionally, Ti K-edge XANES spectra (Supporting Information, Fig. S12) showed a slight blue shift in the Ni-TiO_2-Air compared with pristine Ni-TiO_2 and Ni-TiO_2-N_2, suggesting a relatively reduced valence state of Ti in the sample.

https://doi.org/10.1038/s41467-025-56190-5

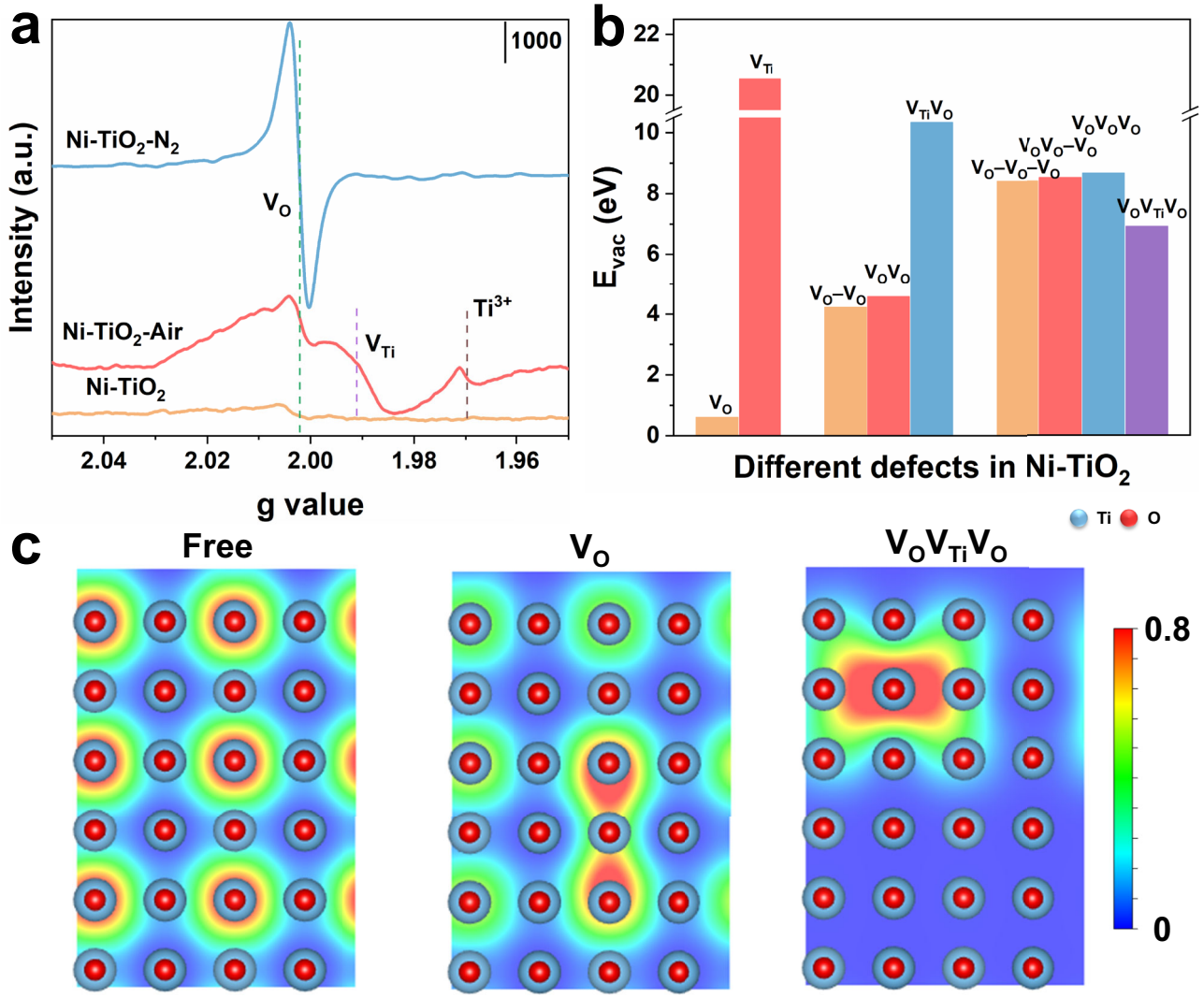

Fig. 2 | Structural characterization of the catalysts. a Low-temperature electron paramagnetic resonance (EPR) of each sample. **b** Formation energies of different defects in Ni-TiO_2. The dashes in V_O–V_O, V_O–V_OV_O and V_O–V_O–V_O represent the segregation of vacancies. **c** Schematic representations of the positron density distributions of the (left) free, (middle) isolated V_O vacancy, and (right) $V_OV_{Ti}V_O$ vacancy associates. The blue and red balls represent the Ti and O atoms, respectively.

Table 1 | Positron lifetime parameters of TiO_2-Air, Ni-TiO_2, Ni-TiO_2-Air, and Ni-TiO_2-N_2

Samples	τ_1[a] (ps)	τ_2[a] (ps)	τ_3[a] (ns)	I_1[b] (%)	I_2[b] (%)	I_3[b] (%)	I_1/I_2
TiO_2-Air	231.8 ± 3.7	370.7 ± 0.3	13.1 ± 2.2	13.7 ± 0.1	86.0 ± 0.1	0.3 ± 0.05	0.16
Ni-TiO_2	197.8 ± 2.2	396.8 ± 1.3	11.1 ± 1.4	31.8 ± 0.4	67.7 ± 0.4	0.5 ± 0.04	0.47
Ni-TiO_2-Air	232.3 ± 4.1	418.4 ± 3.7	5.7 ± 0.2	48.2 ± 1.3	50.8 ± 1.3	1.0 ± 0.03	0.95
Ni-TiO_2-N_2	197.7 ± 4.5	390.3 ± 1.4	10.7 ± 0.5	27.9 ± 0.6	71.1 ± 0.6	1.0 ± 0.03	0.39

[a]The positron lifetimes of different components.
[b]The relative intensities of different lifetime components.

Proposed formation mechanisms

Temperature-programmed surface reaction (TPSR) measurements were conducted to investigate how annealing atmospheres affected the formation of various defects in Ni-TiO_2. As depicted in Fig. 4a, Ni-TiO_2-Air displayed more intense CO and H_2O desorption peaks than Ni-TiO_2-N_2 at 180–300 °C, indicating a more pronounced decomposition of organic residuals at the surface[21]. Similar phenomenon was observed in thermogravimetric analyses (TGA) (Fig. S13). In situ diffuse reflectance infrared Fourier transform spectroscopy (DRIFTS) (Fig. S14) further indicated that the pristine Ni-TiO_2 possessed distinct lactate species (or derived from them) at surface, originating from the TiBALD precursor. These lactate species were gradually decomposed at elevated temperatures under air and N_2 annealing, leading to the formation of H_2O, CO_2 and CO, consistent with the TPSR results (Fig. 4a).

As reported[31], the desorbed water at 100–300 °C mainly originates from the dehydration of labile hydroxyl groups (e.g., clusters, terminal ones, and doubly bridging ones). To distinguish these

https://doi.org/10.1038/s41467-025-56190-5

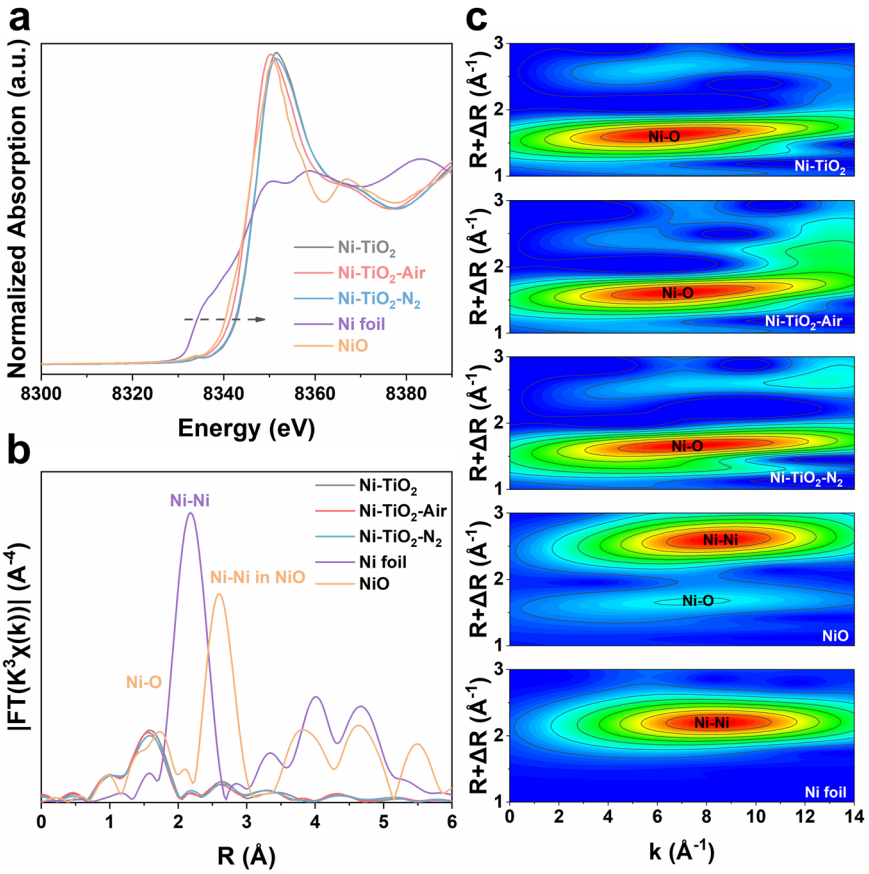

Fig. 3 | Chemical environment of the catalysts. a Normalized Ni K-edge X-ray absorption near-edge structure (XANES) spectra and **b** Fourier transform of extended X-ray absorption fine structure (FT-EXAFS) spectra of Ni-TiO_2, Ni-TiO_2-Air, Ni-TiO_2-N_2, Ni foil, and NiO. **c** Wavelet transform (WT) of EXAFS spectra of Ni foil, NiO, Ni-TiO_2, Ni-TiO_2-Air, and Ni-TiO_2-N_2. *R* represents the average distance between atoms, while *k* represents the wave vector of the photoelectron.

hydroxyl groups in Ni-TiO_2-N_2 and Ni-TiO_2-Air, in situ DRIFTS was conducted, which indicated that annealing in air and N_2 both yielded surface bridging (acidic OH_{br}, ca. 3675 and 3647 cm^{-1}) and terminal (basic OH_{te}, ca. 3692 and 3713 cm^{-1}) hydroxyl groups in the samples[32–34], while at elevated temperatures, the OH_{br} increased gradually, and the OH_{te} was consumed and disappeared at the temperature ≥ 180 °C (since its DRIFTS differential spectra remained nearly unchanged above this temperature), suggesting that OH_{te} is more labile than OH_{br} (Fig. 4b). Pyridine-IR measurements further showed that air annealing did not affect the Brønsted acidity of Ni-TiO_2, whereas N_2 annealing significantly increased this acidity due to the abundant generation of acidic OH_{br} (Fig. 4c and Table S6). Interestingly, Ni atom doping was shown to inhibit the formation of OH_{br}, as the calcination of TiO_2 in air increased the Brønsted acidity, while the calcination of Ni-TiO_2 in air did not result in such an increase.

To explore the essential role of surface hydroxyl groups in facilitating the formation of various defects in Ni-TiO_2, we then calculated the formation energy of $V_OV_{Ti}V_O$ in the $NiTi_{23}O_{28}$ slab in the presence of bridging (OH_{br}) and terminal (OH_{te}) hydroxyl groups (Fig. 4d). We found that OH_{br} adsorption at cationic Ni and Ti sites slightly reduces the E_{vac} of $V_OV_{Ti}V_O$ from 6.92 to 6.44 eV, whereas OH_{te} adsorption at cationic Ti sites renders the formation of $V_OV_{Ti}V_O$ energetically favorable, with an E_{vac} of only −1.12 eV. These results indicate that OH_{te} adsorbed at unsaturated cationic sites significantly enhances the formation of $V_OV_{Ti}V_O$ in Ni-TiO_2, thereby elucidating the diverse defect configurations observed in organic-coated Ni-TiO_2 upon air and N_2 annealing. Further Bader charge analysis (Supporting Information, Fig. S15) revealed that electrons from adjacent OH_{br} were transferred to O–Ti–O associates (0.03 e), while electrons from O–Ti–O associates were transferred to nearby OH_{te} (0.36 e). The latter resulted in a much easier migration of O–Ti–O associates from the bulk Ni-TiO_2 lattice, boosting the formation of $V_OV_{Ti}V_O$. This phenomenon has also been observed by Wang et al.[35], whereas steam treatment of TiO_2 with 75 vol% H_2O/N_2 at 600 °C can efficiently result in O–Ti–O migration onto Au NPs, forming an oxygen-saturated TiO_2 overlayer.

We proposed that during N_2 annealing, the O_2-deficient atmosphere led to the lack of O atom to fulfill the oxygen vacancy as generated by the decomposition of surface-bonding organics at TiO_2 surface. This led to the formation of abundant monovacancies (V_O) sites. Consequently, the generated H_2O (as confirmed by TPSR analyses) tended to be dissociated at V_O site, leading to the formation of stable OH_{br}, which yielded the Ni–O coordination numbers (5.96) of Ni-TiO_2-N_2 nearly identical to that of pristine Ni-TiO_2 (6.00) as confirmed by EXAFS analyses (Fig. S11). While for air annealing, the O_2-rich atmosphere could reduce the likelihood of V_O formation through an O_2-fullfill process. This could benefit the formation of OH_{te} at initial annealing stage, facilitating the generation of $V_OV_{Ti}V_O$ at elevated temperatures. Since the OH_{te} is unstable that can be fully desorbed at ≥180 °C as confirmed by DRIFTS and additional TGA measurements, the $V_OV_{Ti}V_O$ vacancy associates in the Ni-TiO_2-Air would not be occupied by the OH_{te}, thus showing a lower Ni–O coordination numbers (5.31) than that of Ni-TiO_2 (6.00). The proposed whole process was shown in Fig. S16.

To further investigate the potential influence of the generated CO on the formation of $V_OV_{Ti}V_O$ in Ni-TiO_2, the E_{vac} in the presence of CO was also calculated. CO preferentially adsorbs at unsaturated cationic Ti sites, reducing E_{vac} to 4.85 eV, which is much greater than that of OH_{te}, thus confirming the dominant role of OH_{te} in promoting the

https://doi.org/10.1038/s41467-025-56190-5

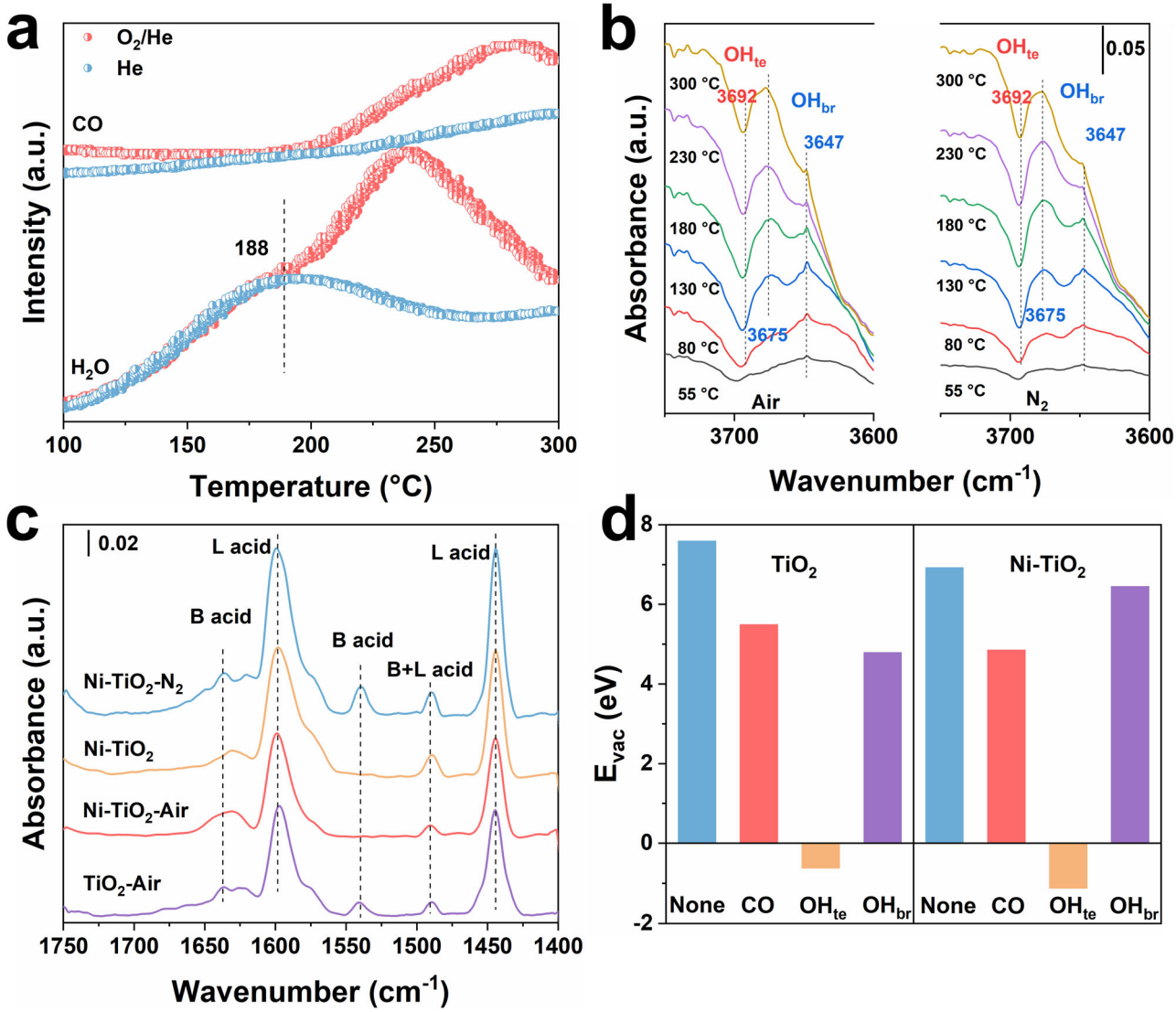

Fig. 4 | Triple vacancy associates $V_OV_{Ti}V_O$ formation mechanism study. **a** Temperature-programmed surface reaction (TPSR) measurements of Ni-TiO_2 in O_2/He and He atmospheres. **b** In situ diffuse reflectance infrared Fourier transform spectroscopy (DRIFTS) differential spectra of the Ni-TiO_2 sample recorded at various ramping temperatures and after being treated for 1 h at 300 °C. The reaction atmosphere was air or N_2. The differential absorbance spectra are obtained by subtracting the initial absorbance spectrum (30 °C) from the absorbance spectrum at the measurement time. **c** Pyridine-IR spectra of TiO_2-Air, Ni-TiO_2, Ni-TiO_2-Air and Ni-TiO_2-N_2 samples. **d** Triple vacancy associates $V_OV_{Ti}V_O$ formation energy in TiO_2 and Ni-TiO_2 samples under different conditions.

formation of $V_OV_{Ti}V_O$. Importantly, a previous study showed that organic-coated SnO_2 annealed in a He atmosphere was also characterized by the presence of anion–cation vacancy associates[36]. This may imply that the function of OH_{te} in generating anion–cation vacancy associates could be applicable for other metal oxides.

H_2O activation ability

Subsequently, we investigated the process of H_2O dissociation and site regeneration on the monovacancy (V_O) and triple vacancy associates ($V_OV_{Ti}V_O$) in Ni-TiO_2. Bader charge analysis (Supporting Information, Fig. S17) revealed that in the $NiTi_{23}O_{28}$ slab, electrons from the Ni atoms were transferred to adjacent oxygen atoms. The presence of V_O resulted in the migration of 0.31 e from Ni to O, whereas $V_OV_{Ti}V_O$ led to the migration of 0.08 e to O. The adsorption of OH_{br} adjacent to the Ni atom with V_O and $V_OV_{Ti}V_O$ both resulted in an increase of ~0.1 e migration from the Ni (Supporting Information, Fig. S18). According to our in situ DRIFTS and pyridine-IR results, Ni-TiO_2-N_2 possessed abundant OH_{br} at the surface compared to Ni-TiO_2-Air, which can induce many more electrons to migrate from Ni, thereby causing an increase in the chemical valence of Ni. This finding is consistent with the XANES and quasi in situ XPS results. The energies of H_2O adsorption (E_{ads}) and dissociation (E_{act}) on V_O and $V_OV_{Ti}V_O$ in the $NiTi_{23}O_{28}$ slab were then calculated. Bader charge analysis and differential charge density calculations indicated more electron transfer from H_2O to the $V_OV_{Ti}V_O$ sites, showing an increase in the bonding strength with H_2O molecules (Supporting Information, Fig. S19)[37,38]. The resulting surface OH* bonded to coordinatively unsaturated Ni atoms, leading to the formation of surface OH* and $O_{lat}H$* (Supporting Information, Figs. S20, S21). However, the E_{act} of $NiTi_{23}O_{28}$-1V_O was calculated to be only −0.02 eV, which is significantly lower than that for $NiTi_{23}O_{28}$-$V_OV_{Ti}V_O$ (0.33 eV) (Fig. 5a), suggesting that H_2O dissociation is energetically more favorable at the V_O site than at the $V_OV_{Ti}V_O$ site. This is contrary to our subsequent in situ DRIFTS measurements (with saturated H_2O vapor at 30 mL min^{-1}, 30 °C, Fig. 5b), which revealed that the band intensity ratio of generated OH* at 3692 cm^{-1} to adsorbed H_2O at 1625 cm^{-1} (I_{OH}) in Ni-TiO_2-Air doubled compared to that of Ni-TiO_2-N_2 (Fig. 5c), suggesting a much greater H_2O activation capability for Ni-TiO_2-Air[14,39].

https://doi.org/10.1038/s41467-025-56190-5

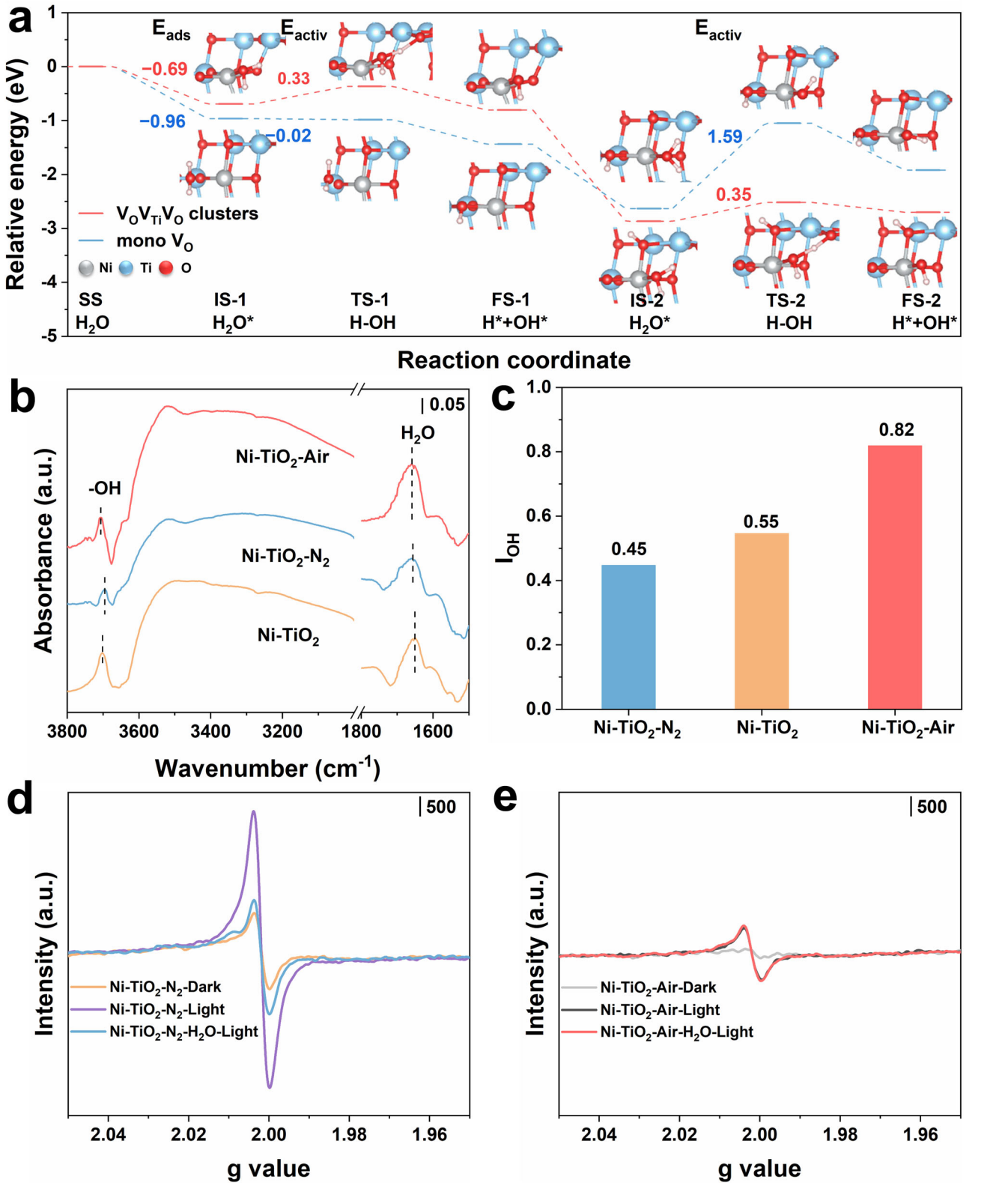

Fig. 5 | Promotion role of $V_OV_{Ti}V_O$ in H_2O activation. a The energy change for the first and second H_2O molecule dissociations on $NiTi_{23}O_{28}$-$V_OV_{Ti}V_O$ (vacancy associates) and $NiTi_{23}O_{28}$-$1V_O$ (monovacancy) slabs. **b** In situ DRIFTS spectra of H_2O adsorption and **c** band intensity ratio of surface OH*/adsorbed H_2O (I_{OH}). In situ EPR spectra of Ni-TiO_2-N_2 (**d**) and Ni-TiO_2-Air (**e**) under different conditions.

To understand this inconsistency, defect regeneration behaviors for V_O and $V_OV_{Ti}V_O$ were investigated. As shown in Fig. S22, the desorption energy (E_{des}) of OH* (the cleavage of Ni–OH*) from $NiTi_{23}O_{28}$-$1V_O$ was calculated at 5.06 eV, which is significantly greater than that of 1.69 eV from $NiTi_{23}O_{28}$-$V_OV_{Ti}V_O$, suggesting that V_O is inclined to be blocked during the H_2O continual activation cycle. Our in situ EPR measurements under saturated H_2O (flow rate at 30 mL min^{-1}, −150 °C, with $\lambda \geq 320$ nm light irradiation) further confirmed that the continual

addition of saturated H_2O significantly decreased the abundance of oxygen vacancies ($g = 2.002$) in Ni-TiO_2-N_2 (Fig. 5d), despite the increase in oxygen vacancies under light irradiation. In contrast, Ni-TiO_2-Air showed no significant change in vacancy abundance after light irradiation (Fig. 5e), exhibiting a high capacity for continual H_2O activation.

When the second H_2O molecule was introduced, the surface OH* on $NiTi_{23}O_{28}$-$1V_O$ tended to occupy the original oxygen vacancy adjacent to the Ni ions. In contrast, for $NiTi_{23}O_{28}$-$V_OV_{Ti}V_O$, the surface geometry of the original Ni–OH* was well preserved (Supporting Information, Figs. S20, S21). The well-preserved surface coordinatively unsaturated Ni atoms can further dissociate the second H_2O with high resistance to surface reconstruction by hydroxyl groups. The energy of the second H_2O dissociation (E'_{act}) on $NiTi_{23}O_{28}$-$V_OV_{Ti}V_O$ showed a similar E'_{activ} of 0.35 eV to that of the first H_2O E_{act} (at 0.33 eV), while $NiTi_{23}O_{28}$-$1V_O$ exhibited a significantly increased E'_{activ} of 1.59 eV, which drastically deviated from that of the first cycle (at −0.02 eV). Based on our aforementioned results, it can be concluded that vacancy associates ($V_OV_{Ti}V_O$) can maintain continual H_2O dissociation owing to the easy regeneration of active defect sites, while monovacancies (V_O) can be easily saturated by the accumulation of dissociative bridging hydroxyls (OH_{br}), leading to the gradual depletion of active sites. This explains the inconsistency between the H_2O dissociation ability and continual activation performance for Ni-TiO_2-N_2 and Ni-TiO_2-Air.

Performance measurements

Photocatalytic HER and hydrodechlorination (HDC) were then conducted to confirm the advancements in associated defect engineering in H_2O continual activation. As shown in Supplementary Fig. S23a, Ni-TiO_2-Air outperformed Ni-TiO_2-N_2 in both reactions, with an ~3.3-fold increase for the HDC and a 6.8-fold increase for the HER. The photocatalytic activity of Ni-TiO_2-Air was also greater than that of well-designed noble metal-doped TiO_2 catalysts under similar reaction conditions[40]. After four successive catalytic cycles (Supporting Information, Fig. S23b), Ni-TiO_2-Air exhibited high stability and reusability, retaining its crystal structure and surface valence (Supporting Information, Fig. S24).

One may argue that the light absorption and charge separation/transfer behaviors can also affect the photocatalytic performances of the Ni-TiO_2-Air and Ni-TiO_2-N_2 samples. To clarify these effects, we investigated the solar light harvesting efficiency using ultraviolet–visible diffuse reflection spectroscopy (UV–Vis DRS), EPR in the presence of 2,2,6,6-tetramethylpiperidine-1-oxyl (TEMPO, as a spin trap), transient photocurrent curves, and electrochemical impedance spectroscopy (Supporting Information, Figs. S25–S28). These analyses all revealed that Ni-TiO_2-N_2 exhibited superior optical utilization efficiency and charge transfer kinetics compared to those of Ni-TiO_2-Air. This is consistent with previous work by Liu et al.[33], who showed that introducing OH_{br} onto anatase TiO_2 (analogous to our Ni-TiO_2-N_2) can narrow its bandgap, enhance its light response, and facilitate photogenerated charge carrier transfer. Moreover, there are no obvious differences in the phase structures (Figs. S2, S3 and Table S2) and specific surface areas (Table S3) between Ni-TiO_2-Air and Ni-TiO_2-N_2 (Table S7). The inconsistency between the inherent photocatalytic properties and photocatalytic performances of Ni-TiO_2-Air and Ni-TiO_2-N_2 underscores the critical role of associated defects in H_2O continual activation for photocatalytic HER and HDC reactions.

To further reveal the role of $V_OV_{Ti}V_O$ vacancy associates, experiments for controlling the amounts of triple O–Ti–O vacancy associates were conducted by varying the annealing temperature (200 °C, 300 °C, 400 °C). The photocatalytic activities of each sample in the HER and HDC reactions were shown in Fig. S29. Also, the PALS data were shown in Fig. S30 and Table S8. The results demonstrate a volcano-like trend in both the activity of the samples and the corresponding amount of triple O–Ti–O vacancies as the calcination temperature increases, initially rising and then significantly decreasing. This is a notable positive correlation between the photocatalytic activity of the samples and the amount of vacancy clusters present, where Ni-TiO_2-Air-300 (also labeled as Ni-TiO_2-Air) possessing the highest amount of triple O–Ti–O vacancies exhibits the best photocatalytic activity in the HER and HDC reactions. Additionally, to elucidate the effect of residual organics after N_2 annealing, Ni-TiO_2-N_2 was further subjected to air annealing at 300 °C for 2 h (denoted as Ni-TiO_2-N_2-Air), which did not show obvious difference in the photocatalytic activity for the HER and HDC reactions (Fig. S31).

Our experimental and theoretical results demonstrate that the $V_OV_{Ti}V_O$ in the Ni-TiO_2-Air can confer improved structural resilience to facilitate dissociative OH* deprotonation for active site regeneration, thereby ensuring continual H_2O activation for the HER and HDC reactions, while the coordinatively unsaturated metal sites originating from the V_O on Ni-TiO_2-N_2 can be easily saturated by accumulated dissociative OH*, leading to a gradual depletion of active sites.

Discussion

We have developed a notable defect engineering strategy aimed at introducing various vacancy configurations in organic-coated TiO_2 to efficiently enhance H_2O activation catalysis. This strategy involves the incorporation of monodisperse Ni sites and meticulous modulation of the annealing atmosphere. Our investigations, including XAFS and PALS measurements, confirmed the predominance of $V_OV_{Ti}V_O$ vacancy associates in Ni-TiO_2-Air, distinguishing it significantly from Ni-TiO_2-N_2. The generation of OH_{te} during air aging facilitated the formation of $V_OV_{Ti}V_O$, and Ni doping increased their relative abundance. Experimental results, combined with theoretical calculations, revealed the critical role of the defect configuration in H_2O activation. Specifically, vacancy associates $V_OV_{Ti}V_O$ with lower energy barriers for active site regeneration exhibited superior structural resilience to facilitate dissociative OH* deprotonation, thereby promoting continual H_2O activation. The essential role of vacancy associates in H_2O activation was evidenced by the remarkable catalytic performance of Ni-TiO_2-Air in the HER and HDC reactions. This work paves the way for the rational tuning of the predominant vacancy configuration to adjust the electronic structure of active sites in metal oxides. Our findings are expected to inspire further advancements in the development of promising defective catalysts for a wide variety of reactions involving H_2O.

Methods

Materials

Titanium(IV) bis(ammonium lactate)dihydroxide (TiBALD, aqueous, 50% w/w), $Ni(NO_3)_2{\cdot}6H_2O$ (AR, 99%), and $Pd(NO_3)_2{\cdot}2H_2O$ (AR, 99%) were purchased and used without further purification. Deionized water was used in all experiments.

Synthesis of organic-coated Ni-doped TiO_2

Titanium oxide-based NPs were fabricated by using a three-pump CHFS route (Supporting Information, Fig. S1) as described in detail in our previous studies[22,23,41]. For a 1 mol% Ni-doped TiO_2, a solution containing titanium(IV) bis(ammonium lactate)dihydroxide (TiBALD) (0.1 M) and $Ni(NO_3)_2{\cdot}6H_2O$ (0.001 M) was pumped at a rate of 7.5 mL min^{-1} to meet a flow of supercritical water (pumping rate of 30 mL min^{-1}) at the reactor's heating point (via a T-mixer). This led to the rapid nucleation and precipitation of hybrid metal oxides. The resulting mixture was then washed, centrifuged, and dried to obtain the pure phase, designated as Ni-TiO_2[41].

Synthesis of Ni-TiO_2-Air and Ni-TiO_2-N_2

To introduce vacancies, the pristine Ni-TiO_2 powder was further heat-treated at 300 °C (at a heating rate of 3 °C min^{-1}) for 2 h under an air atmosphere. The obtained sample was denoted as Ni-TiO_2-Air. For

comparison, the Ni-TiO_2 sample heated at 300 °C (at a heating rate of 3 °C min^{-1}) for 2 h under a N_2 atmosphere was also prepared and named Ni-TiO_2-N_2. To clarify the role of annealing temperature, the Ni-TiO_2 sample was also heat-treated at 200 °C (labeled as Ni-TiO_2-Air-200) and 400 °C (labeled as Ni-TiO_2-Air-400) (at a heating rate of 3 °C min^{-1}) for 2 h under an air atmosphere, respectively.

Catalyst characterization and catalytic activity measurements

The structural and physicochemical properties of the as-prepared samples were analysed by using a range of analytical techniques. Details of the experimental analysis methods and photoelectrochemical measurements are available in the Supporting Information.

PALS measurements were carried out using a digital spectrometer (TechnoAP, Japan) with a temporal resolution of ~200 ps at full width at half maximum. The prepared sample powder was pressed into disc-shaped pellets with a diameter of 10 mm and a thickness of ~1 mm. A ^{22}Na positron source (~30 μCi), encapsulated between two Kapton polyimide films (0.0075 × 10 × 10 mm), was positioned between two identical pellet-shaped samples. The sample-source-sample assembly was positioned in a chamber that had been evacuated using a turbo molecular pump. The system consisted of 8192 channels, each with a width of 10.417 ps/channel. For each sample, more than 2×10^6 data points were collected at room temperature[42].

The ideal positron lifetime spectrum $L(t)$ is a sum of several exponential decay terms as follows

$$L(t) = \sum_{i=1}^{n} \frac{I_i}{\tau_i} \exp\left(-\frac{t}{\tau_i}\right) \quad (1)$$

where n is the number of lifetime components and I_i is the corresponding intensities for each component. The actual positron lifetime spectrum is a convolution of the above equation with the time resolution $R(t)$ of the lifetime spectrometer as follows

$$Y(t) = L(t) \times R(t) = N_t \sum_{i=1}^{n} \frac{I_i}{\tau_i} \int_0^{\infty} R(t - t') \exp\left(-\frac{t}{\tau_i}\right) dt' + B \quad (2)$$

where N_t is the total counts of the spectrum and B is the background count in the spectrum.

The PALS were well fitted to three lifetime components using the Lifetime9 software. The theoretical positron annihilation lifetimes of TiO_2 with different defect types were calculated based on DFT in the atomic superposition framework implemented in the Quantum ESPRESSO code[43,44]. In the lifetime calculations, the projected augmented wave (PAW), generalized gradient approximation (GGA), and Perdew–Burke–Ernzerhof (PBE) pseudopotentials were employed. This method is widely applied for electronic structure analysis, especially in materials with defects, as reported previously[43,44]. The computational approach referenced the Quantum Monte Carlo (QMC) and GGA methods. This method offers an advanced quantum mechanical treatment, allowing for more accurate descriptions of electronic states and lifetimes related to oxygen vacancies and defects. In this work, a simulation model ($Ti_{48}O_{96}$) was constructed. To calculate the positron annihilation lifetime in an actual situation, the structure with the vacancy defects was fully relaxed.

X-ray absorption fine spectroscopy (XAFS) experiments were performed at the Ni K-edge and Ti K-edge using the 1W1B beamline at the Beijing Synchrotron Radiation Facility (BSRF). Si (111) double crystal monochromators were used to adjust the beam. Calibration of the energy scale was achieved by referencing the absorption edges of pure Ni and Ti foils. The storage ring typically operated at 2.5 GeV with a maximum current of 250 mA. The XAFS data were handled and evaluated using the Demeter software package. The pre-edge region was corrected by subtracting a linear function, after which the edge step was normalized using the Athena software[45].

EPR spectra were recorded on a JEOL JES-FA200 EPR spectrometer (JEOL, Japan) to detect the presence of oxygen vacancies, superoxide radicals (•O_2^-), hydroxyl radicals (•OH) radicals, and photogenerated electrons (e^-) and holes (h^+) in the photocatalytic system under visible light irradiation. Specifically, 5,5-dimethyl-1-pyrroline N-oxide (DMPO, 50 mM) in methanol (•O_2^-) or aqueous (•OH) dispersions and 2,2,6,6-tetramethylpiperidine-1-oxyl (TEMPO, 50 mM) in acetonitrile (h^+) or aqueous (e^-) dispersions were employed as spin traps to detect radicals. In situ EPR spectra were obtained on a JES-FA 200 JOES spectrometer at −150 °C. In the test, the sample (20 mg) was placed in a nuclear magnetic resonance tube and subjected to saturated H_2O (flow rate of 30 mL min^{-1}) for 20 min. The EPR data were then recorded under full spectrum illumination ($\lambda \geq 320$ nm).

The photocatalytic HER and hydrodechlorination (HDC) of trichloroethylene (TCE) activities were evaluated through batch experiments (50 mL of aqueous solution and 160 mL of headspace). The light source was a 300 W Xe lamp (PLS-SXE300, Perfectlight, China). In addition, the temperature of the test was monitored at 25 °C through a water flow in the jacket surrounding the reactor. The irradiation intensity of the photocatalytic reaction was measured to be 3.6 mW cm^{-1} ($\lambda \geq 320$ nm). The details are described in the Supporting Information.

Computational methods

The Vienna Ab Initio Package[46,47] was utilized to perform all the spin-polarized DFT calculations within the GGA[48–51] in the PBE formulation. The ionic cores were described using the PAW potentials[50,51], while the valence electrons were accounted for with a plane wave basis set, having a kinetic energy cut-off of 400 eV. Partial occupancies of the Kohn–Sham orbitals were treated using the Gaussian smearing method, with a width of 0.05 eV. The electronic energy was considered self-consistent when the energy change was less than 10^{-5} eV. Geometry optimization was deemed convergent when the residual forces fell below 0.02 eV $Å^{-1}$. Dispersion interactions were modeled using Grimme's DFT-D3 methodology[52].

The lattice constants of the anatase TiO_2 unit cell were optimized, yielding values of $a = b = 3.858$ Å and $c = 9.652$ Å, using a 10 × 10 × 4 Monkhorst-Pack k-point grid for Brillouin zone sampling. Based on these optimized values, a TiO_2(101) surface model (Model 1) was constructed, with a $p(1 \times 3)$ periodicity in the x and y directions, two stoichiometric layers in the z direction, and a vacuum layer of 15 Å to separate the surface slab from its periodic images. Model 1 contains 24 Ti and 48 O atoms. To create Model 2, a Ni atom was substituted for a Ti atom in the outermost layer of Model 1. The Hubbard parameter was set to U–J = 4.5 eV for Ti to provide an accurate qualitative description of the structure and electronic properties of TiO_2[53,54]. During geometry optimization, a 2 × 2 × 1 k-point grid was used for Brillouin zone sampling, with the bottom stoichiometric layer fixed while the other layers were allowed to relax fully.

The transition state of an elementary reaction step was determined using the climbing image nudged elastic band (CI-NEB) method[55–57]. Details of the DFT calculations are available in the Supporting Information.

Data availability

The data that support the findings of this study are available within the paper and its Supplementary information. Source data of Figs. 2–5 are provided with this paper as a Source Data file. Atomic coordinates of the optimized structure of Figs. 2c and 5a are provided in Supplementary data. Extra data are available from the corresponding author on reasonable request. Source data are provided with this paper.

References

1. Wendt, S. et al. The role of interstitial sites in the Ti3*d* defect state in the band gap of titania. *Science* **320**, 1755–1759 (2008).
2. Ma, J., Long, R., Liu, D., Low, J. & Xiong, Y. Defect engineering in photocatalytic methane conversion. *Small Struct.* **3**, 2100147 (2021).
3. Bai, S., Zhang, N., Gao, C. & Xiong, Y. Defect engineering in photocatalytic materials. *Nano Energy* **53**, 296–336 (2018).
4. Shi, R., Zhao, Y., Waterhouse, G. I. N., Zhang, S. & Zhang, T. Defect engineering in photocatalytic nitrogen fixation. *ACS Catal.* **9**, 9739–9750 (2019).
5. Zhang, Y. et al. Defect engineering in metal sulfides for energy conversion and storage. *Coord. Chem. Rev.* **448**, 214147 (2021).
6. Choi, H. et al. Influence of lattice oxygen on the catalytic activity of blue titania supported Pt catalyst for CO oxidation. *Catal. Sci. Technol.* **11**, 1698–1708 (2021).
7. Li, G. et al. Effect of oxygen vacancies and its quantity on photocatalytic oxidation performance of titanium dioxide for NO removal. *Colloids Surf. A Physicochem. Eng. Asp.* **614**, 126156 (2021).
8. Qian, H. et al. Oxygen vacancy enhanced photocatalytic activity of Cu_2O/TiO_2 heterojunction. *iScience* **27**, 109578 (2024).
9. Oh, S. et al. Oxygen activation on the interface between Pt nanoparticles and mesoporous defective TiO_2 during CO oxidation. *J. Chem. Phys.* **151**, 234716 (2019).
10. Han, T. et al. Photosynthesis of benzonitriles on BiOBr nanosheets promoted by vacancy associates. *Angew. Chem. Int. Ed.* **62**, e202313325 (2023).
11. Li, L. et al. Atom-economical synthesis of dimethyl carbonate from CO_2: engineering reactive frustrated lewis pairs on ceria with vacancy clusters. *Angew. Chem. Int. Ed.* **61**, e202214490 (2022).
12. Wang, W., Zhang, W., Deng, C., Sheng, H. & Zhao, J. Accelerated photocatalytic carbon dioxide reduction and water oxidation under spatial synergy. *Angew. Chem. Int. Ed.* **63**, e202317969 (2024).
13. Guan, M. et al. Vacancy associates promoting solar-driven photocatalytic activity of ultrathin bismuth oxychloride nanosheets. *J. Am. Chem. Soc.* **135**, 10411–10417 (2013).
14. Wei, Z. et al. Oxygen vacancy-engineered titanium-based perovskite for boosting H_2O activation and lower-temperature hydrolysis of organic sulfur. *Proc. Natl Acad. Sci. USA* **120**, e2217148120 (2023).
15. Yao, S. et al. Atomic-layered Au clusters on α-MoC as catalysts for the low-temperature water-gas shift reaction. *Science* **357**, 389–393 (2017).
16. Sun, S. et al. Photoinduced composite of Pt decorated $Ni(OH)_2$ as strongly synergetic cocatalyst to boost H_2O activation for photocatalytic overall water splitting. *Appl. Catal. B Environ.* **243**, 253–261 (2019).
17. Mahmood, J. et al. An efficient and pH-universal ruthenium-based catalyst for the hydrogen evolution reaction. *Nat. Nanotechnol.* **12**, 441–446 (2017).
18. Zhu, J., Hu, L., Zhao, P., Lee, L. Y. S. & Wong, K.-Y. Recent advances in electrocatalytic hydrogen evolution using nanoparticles. *Chem. Rev.* **120**, 851–918 (2019).
19. Zhang, R. et al. Tracking the role of defect types in Co_3O_4 structural evolution and active motifs during oxygen evolution reaction. *J. Am. Chem. Soc.* **145**, 2271–2281 (2023).
20. Fujishima, A. & Honda, K. Electrochemical photolysis of water at a semiconductor electrode. *Nature* **238**, 37–38 (1972).
21. Chen, J. et al. Palladium encapsulated by an oxygen-saturated TiO_2 overlayer for low-temperature SO_2-tolerant catalysis during CO oxidation. *Angew. Chem. Int. Ed.* **62**, e202310191 (2023).
22. Bi, F. et al. Vacancy-defect semiconductor quantum dots induced an S-scheme charge transfer pathway in 0D/2D structures under visible-light irradiation. *Appl. Catal. B Environ.* **306**, 121109 (2022).
23. Weng, X. et al. Thermocatalytic syntheses of highly defective hybrid nano-catalysts for photocatalytic hydrogen evolution. *J. Mater. Chem. A* **5**, 23766–23775 (2017).
24. Wang, S. et al. Titanium-defected undoped anatase TiO_2 with p-type conductivity, room-temperature ferromagnetism, and remarkable photocatalytic performance. *J. Am. Chem. Soc.* **137**, 2975–2983 (2015).
25. Pan, L. et al. Manipulating spin polarization of titanium dioxide for efficient photocatalysis. *Nat. Commun.* **11**, 418 (2020).
26. Liang, L. et al. Atmospheric CO_2 capture and photofixation to near-unity CO by Ti^{3+}-Vo-Ti^{3+} sites confined in TiO_2 ultrathin layers. *Sci. China Chem.* **64**, 953–958 (2021).
27. Meng, Q. et al. In situ valence modification of Pd/NiO nano-catalysts in supercritical water towards toluene oxidation. *Catal. Sci. Technol.* **8**, 1858–1866 (2018).
28. Xiong, L. et al. Highly selective transformation of biomass derivatives to valuable chemicals by single-atom photocatalyst Ni/TiO_2. *Adv. Mater.* **35**, e2209646 (2023).
29. Song, H. et al. Atomically dispersed nickel anchored on a nitrogen-doped carbon/TiO_2 composite for efficient and selective photocatalytic CH_4 oxidation to oxygenates. *Angew. Chem. Int. Ed.* **62**, e202215057 (2023).
30. Jia, G. et al. Asymmetric coupled dual-atom sites for selective photoreduction of carbon dioxide to acetic acid. *Adv. Funct. Mater.* **32**, 2206817 (2022).
31. Weng, X. et al. Catalytic oxidation of chlorinated organics over lanthanide perovskites: effects of phosphoric acid etching and water vapor on chlorine desorption behavior. *Environ. Sci. Technol.* **53**, 884–893 (2018).
32. Pan, L., Zou, J.-J., Zhang, X. & Wang, L. Water-mediated promotion of dye sensitization of TiO_2 under visible light. *J. Am. Chem. Soc.* **133**, 10000–10002 (2011).
33. Liu, B. et al. Effective regulation of surface bridging hydroxyls on TiO_2 for superior photocatalytic activity via ozone treatment. *Appl. Catal. B Environ.* **304**, 120952 (2022).
34. Li, Y. et al. Dynamic structure of active sites in ceria-supported Pt catalysts for the water gas shift reaction. *Nat. Commun.* **12**, 914 (2021).
35. Wang, H. et al. Oxygen-saturated strong metal-support interactions triggered by water on titania supported catalysts. *Adv. Funct. Mater.* **33**, 2304303 (2023).
36. Liu, L., Shu, S., Zhang, G. & Liu, S. Highly selective sensing of C_2H_6O, HCHO, and C_3H_6O gases by controlling SnO_2 nanoparticle vacancies. *ACS Appl. Nano Mater.* **1**, 31–37 (2018).
37. Li, F. et al. Balancing hydrogen adsorption/desorption by orbital modulation for efficient hydrogen evolution catalysis. *Nat. Commun.* **10**, 4060 (2019).
38. Li, H. et al. High-rate CO_2 electroreduction to C_{2+} products over a copper-copper iodide catalyst. *Angew. Chem. Int. Ed.* **60**, 14329–14333 (2021).
39. Shangguan, W. et al. Molecular-level insight into photocatalytic CO_2 reduction with H_2O over Au nanoparticles by interband transitions. *Nat. Commun.* **13**, 3894 (2022).
40. Xiao, M. et al. Molten-salt-mediated synthesis of an atomic nickel Co-catalyst on TiO_2 for improved photocatalytic H_2 evolution. *Angew. Chem. Int. Ed.* **59**, 7230–7234 (2020).
41. Bi, F., Meng, Q., Zhang, Y., Weng, X. & Wu, Z. Defect engineering in 0D/2D S-scheme heterojunction photocatalysts for water activation: synergistic roles of nickel doping and oxygen vacancy. *ACS Appl. Mater. Interfaces* **15**, 31409–31420 (2023).
42. Zhu, K. et al. Defect engineering on V_2O_3 cathode for long-cycling aqueous zinc metal batteries. *Nat. Commun.* **12**, 6878 (2021).
43. Zhang, W., Gu, B., Liu, J. & Ye, B. Accurate theoretical prediction on positron lifetime of bulk materials. *Comput. Mater. Sci.* **105**, 32–38 (2015).

44. Dong, Y. et al. Quantum Monte Carlo study of correlation energy and pair correlation function at various electron-positron density ratios: accurate calculation of positron annihilation lifetimes in solids. *Phys. Rev. B* **109**, 104104 (2024).
45. Ravel, B. & Newville, M. *ATHENA,ARTEMIS,HEPHAESTUS*: data analysis for X-ray absorption spectroscopy using *IFEFFIT*. *J. Synchrotron. Radiat.* **12**, 537–541 (2005).
46. Kresse, G. & Furthmüller, J. Efficiency of ab-initio total energy calculations for metals and semiconductors using a plane-wave basis set. *Comput. Mater. Sci.* **6**, 15–50 (1996).
47. Kresse, G. & Furthmüller, J. Efficient iterative schemes for ab initio total-energy calculations using a plane-wave basis set. *Phys. Rev. B* **54**, 11169–11186 (1996).
48. Perdew, J. P., Burke, K. & Ernzerhof, M. Generalized gradient approximation made simple. *Phys. Rev. Lett.* **77**, 3865–3868 (1996).
49. Hammer, B., Hansen, L. B. & Nørskov, J. K. Improved adsorption energetics within density-functional theory using revised Perdew-Burke-Ernzerhof functionals. *Phys. Rev. B* **59**, 7413–7421 (1999).
50. Blochl, P. E. Projector augmented-wave method. *Phys. Rev. B* **50**, 17953–17979 (1994).
51. Kresse, G. & Joubert, D. From ultrasoft pseudopotentials to the projector augmented-wave method. *Phys. Rev. B* **59**, 1758–1775 (1999).
52. Grimme, S., Antony, J., Ehrlich, S. & Krieg, H. A consistent and accurate ab initio parametrization of density functional dispersion correction (DFT-D) for the 94 elements H-Pu. *J. Chem. Phys.* **132**, 154104 (2010).
53. Ganduglia-Pirovano, M. V., Hofmann, A. & Sauer, J. Oxygen vacancies in transition metal and rare earth oxides: Current state of understanding and remaining challenges. *Surf. Sci. Rep.* **62**, 219–270 (2007).
54. Peng, Y. et al. Deactivation and regeneration of a commercial SCR catalyst: Comparison with alkali metals and arsenic. *Appl. Catal. B Environ.* **168-169**, 195–202 (2015).
55. Henkelman, G. A., Uberuaga, B. P. & Jónsson, H. A climbing image nudged elastic band method for finding saddle points and minimum energy paths. *J. Chem. Phys.* **113**, 9901–9904 (2000).
56. Henkelman, G. & Jónsson, H. Improved tangent estimate in the nudged elastic band method for finding minimum energy paths and saddle points. *J. Chem. Phys.* **113**, 9978–9985 (2000).
57. Sheppard, D. & Henkelman, G. Paths to which the nudged elastic band converges. *J. Comput. Chem.* **32**, 1769–1771 (2011).

Acknowledgements

We gratefully acknowledge the National Natural Science Foundation of China (No. 52070168, 22176169), and the Key R&D Plan of Zhejiang Province (No. 2023C03127). We thank Dr. Min Jiang (Hangzhou Normal University) for his help with the in situ EPR measurements. We thank Dr. Peirong Chen and Mr. Huibin Liu (South China University of Technology) for their help with the quasi in situ XPS measurements. We also thank Mr. Sibo Zhan (Zhejiang University) for his assistance with the Rietveld refinement of the XRD data.

Author contributions

F.B. and Q.J.M. carried the experiments and analyzed the results. Y.L.Z. performed the catalyst characterization. Q.H.L. collected and analyzed the XAFS data. H.C. and H.J.Z. collected and analyzed the PAS data. B.Q.J., H.F.L., and Z.B.W. supported in assisting with interpreting some of the analytical data and assisting in writing the manuscript. X.L.W., F.B., and Q.J.M. conceived the idea and wrote the paper. X.L.W. supervised the project. All authors discussed the results and assisted during manuscript preparation.

Competing interests

The authors declare no competing interests.

Additional information

Supplementary information The online version contains supplementary material available at https://doi.org/10.1038/s41467-025-56190-5.

Correspondence and requests for materials should be addressed to Xiaole Weng.

Peer review information *Nature Communications* thanks anonymous reviewer(s) for their contribution to the peer review of this work. A peer review file is available.

Reprints and permissions information is available at http://www.nature.com/reprints

Publisher's note Springer Nature remains neutral with regard to jurisdictional claims in published maps and institutional affiliations.

Open Access This article is licensed under a Creative Commons Attribution-NonCommercial-NoDerivatives 4.0 International License, which permits any non-commercial use, sharing, distribution and reproduction in any medium or format, as long as you give appropriate credit to the original author(s) and the source, provide a link to the Creative Commons licence, and indicate if you modified the licensed material. You do not have permission under this licence to share adapted material derived from this article or parts of it. The images or other third party material in this article are included in the article's Creative Commons licence, unless indicated otherwise in a credit line to the material. If material is not included in the article's Creative Commons licence and your intended use is not permitted by statutory regulation or exceeds the permitted use, you will need to obtain permission directly from the copyright holder. To view a copy of this licence, visit http://creativecommons.org/licenses/by-nc-nd/4.0/.

© The Author(s) 2025